Energy Storage Materials 86 (2026) 104997

Contents lists available at ScienceDirect

Energy Storage Materials

journal homepage: www.elsevier.com/locate/ensm

BMINN: Learning chemical potentials and parameters from voltage data for multi-phase battery modeling☆

Yicun Huang [a], Qingbo Zhu [a], Torsten Wik [a], Donal P. Finegan [b], Yang Li [a,c], Changfu Zou [a,*]

[a] Department of Electrical Engineering, Chalmers University of Technology, Gothenburg, 412 96, Sweden
[b] National Renewable Energy Laboratory, 15013 Denver West Parkway, Golden, CO 80401, USA
[c] School of Electrical Engineering and Automation, Wuhan University, Wuhan 430072, China

ARTICLE INFO

Keywords:
Lithium ion battery
Energy modeling
Operando XRD
Machine learning

ABSTRACT

Free-energy landscapes and chemical potentials govern the dynamics of phase transitions, transport, and stability in functional materials, yet they remain experimentally inaccessible under realistic operating conditions. Here we introduce a Bayesian model-integrated neural network (BMINN) that embeds physics-based formulations of non-autonomous partial differential–algebraic equations into probabilistic learning. This approach reconstructs hidden thermodynamics directly from macroscopic current–voltage data, providing quantitative access to metastable states, staging transitions, and energy barriers without synchrotron probes. Demonstrated on lithium–graphite electrodes, BMINN recovers full Gibbs free-energy landscapes with fidelity validated against *operando* X-ray diffraction. The framework generalizes across dynamical regimes, enabling accurate voltage prediction, internal state estimation, and inference of governing parameters. Beyond batteries, BMINN exemplifies a broadly applicable strategy for learning missing physics in multiphase, non-equilibrium systems, offering a new pathway to uncover hidden thermodynamic functions across condensed matter and materials physics.

1. Introduction

The evolution of many-body systems out of equilibrium is governed by hidden thermodynamic functions that determine phase transitions, metastability, and kinetics. From ferroelectric switching to catalytic reactions and ion intercalation in solids, these free-energy landscapes dictate both macroscopic behavior and microscopic pathways. Yet direct measurement of such landscapes under realistic operating conditions remains elusive. Experimental probes such as operando X-ray diffraction (XRD) [1,2], neutron scattering [3], and nuclear magnetic resonance (NMR) [4] can resolve phase transitions in detail, but they require synchrotron or reactor access, custom cell designs, and carefully controlled environments. These requirements make them unsuitable for large-scale or high-throughput characterization. As a result, most modeling approaches rely on open-circuit potential fitting or empirical free-energy expressions, which cannot capture metastable states, interfacial energy barriers, or rate-dependent phase separation [5,6]. This limitation constrains our ability to build predictive models and hinders fundamental understanding of multiphase, non-equilibrium systems.

Graphite, the most widely used negative electrode material in commercial lithium-ion batteries, offers a particularly rich case study of this challenge. During lithiation and delithiation, graphite undergoes a sequence of staging transitions that are conventionally described in terms of the average number of graphene layers between lithium layers. The two classic interpretations of these structures are the Rüdorff–Hoffmann [7] and the Daumas–Hérold [8] models. Each stage corresponds to a local minimum in Gibbs free energy, while intermediate stoichiometries align with miscibility gaps in the chemical potential. Within these gaps, two or more phases coexist, separated by moving interfaces whose dynamics are driven by overpotential. The height of the free-energy barriers plays a decisive role, since experimental observations indicate that some transitions can lag behind others under high intercalation rates [1]. Accurate descriptions of the Gibbs free energy and chemical potential are therefore required to predict phase-boundary migration, to track transient phase populations, and to assess conditions under which parasitic lithium plating is likely to occur.

☆ This work was supported by European Union's Horizon Europe programme under the Marie Skłodowska-Curie Actions Postdoctoral Fellowships (Grant No. 101068764), Marie Skłodowska-Curie Actions (Grant No. 101131278), and the Swedish Research Council (Grant No. 2023-04314).

* Correspondence to: Hörsalsvägen 11, SE 412 96 Gothenburg, Sweden.
E-mail address: changfu.zou@chalmers.se (C. Zou).

https://doi.org/10.1016/j.ensm.2026.104997
Received 6 December 2025; Received in revised form 30 January 2026; Accepted 14 February 2026
Available online 24 February 2026

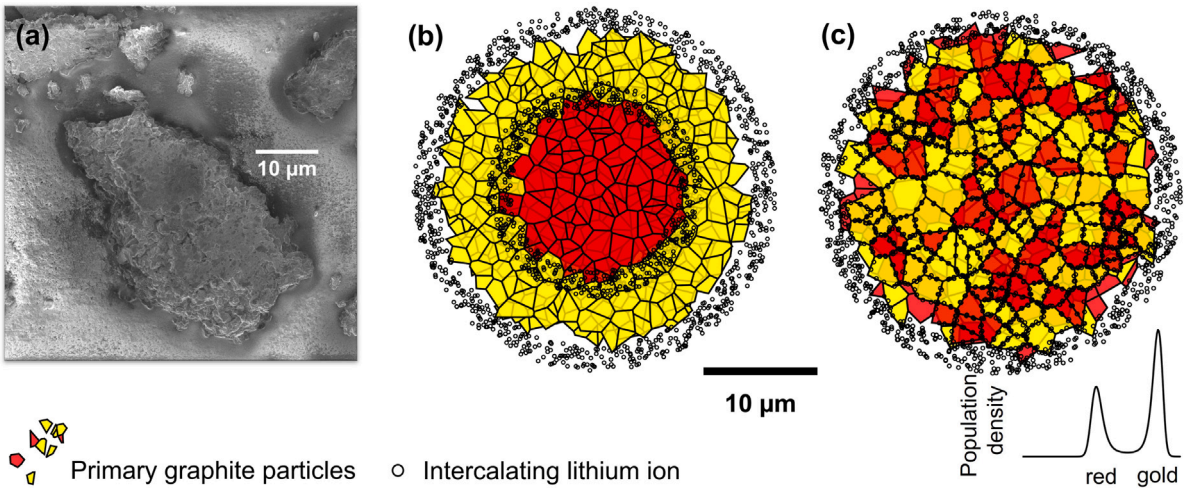

Fig. 1. Hierarchical microstructure of a graphite particle. (a) SEM image of a secondary polycrystalline particle of synthetic graphite. (b) A diffusion-limited picture for the secondary polycrystalline particle. (c) A reaction-limited picture of the primary, single-crystalline particles. During phase transitions, the ensemble of primary particles separates into two phases; for example, a Stage 2–1 transition is characterized by a bimodal population density with two peaks centered around the red phase and gold phase. Experimentally, both phase morphologies have been observed in a graphite electrode [16] under the same operational condition, implying that both diffusion-limited and reaction-limited physical pictures are plausible.

Existing free-energy models illustrate both the progress made and the limitations that remain. For two-phase compounds such as $LiFePO_4$, a one-dimensional double-well function is sufficient to represent phase separation [6,9]. For graphite, Smith et al. [10] proposed a two-dimensional free-energy model consistent with the Rüdorff–Hoffmann bilayer structure, which combines two regular-solution free energies to represent alternating lithium layers, but captures only the Stage 2–1 transition. Chandesris et al. [11,12] extended this model by incorporating the short-range periodicity of the Daumas–Hérold structure, which enables the description of additional stages and transitions. More recently, Ombrini et al. [13] introduced an extended regular-solution model for multi-sublattice compounds such as $LiMn_yFe_{1-y}PO_4$, and Pozzato et al. [14] demonstrated a hybrid physics–machine learning model for $LiFePO_4$–graphite systems. While these approaches effectively capture the major voltage plateaus for single-crystal particles, their applicability to realistic electrodes remains uncertain. Electrodes in practical cells are composed of polycrystalline graphite particles with hierarchical microstructures [15], and electrode-level simulations based on volume-averaging or coarse-graining fail to capture the transient and spatially heterogeneous intercalation behavior observed during real-world cycling [1].

Here we introduce a general inference framework, the Bayesian model-integrated neural network (BMINN), which reconstructs electrode-specific chemical potentials and Gibbs free energies directly from routine current–voltage data. Unlike conventional approaches that rely on predefined functional forms, BMINN embeds multiphase electrode models into a probabilistic learning framework, enabling the recovery of full free-energy landscapes together with quantified uncertainty. Applied to graphite, the reconstructed thermodynamics reproduce *operando* XRD observations, resolve staging dynamics and heterogeneous lithiation pathways, and capture free-energy barriers underlying lagging phase transitions at high rates. More broadly, the framework addresses a general physics problem: learning missing thermodynamics in multiphase, non-autonomous dynamical systems from limited macroscopic observables. In this sense, BMINN provides a methodology that extends well beyond electrochemistry, with potential applications to catalytic surfaces, ferroic materials, and other non-equilibrium systems where hidden free-energy landscapes govern macroscopic performance and stability.

2. Results

2.1. Framework overview

Physical picture. To reconstruct electrode thermodynamics from cycling data, it is first necessary to understand how lithium ions intercalate into graphite electrodes. Yet, the intercalation mechanism remains debated. Traditionally, lithium intercalation has been regarded as diffusion-limited under typical battery operating conditions, a view supported by the core–shell phase separations commonly observed in graphite electrodes [16,17]. The extent of diffusion limitation is influenced by various factors, including C-rate, particle size, geometry, surface morphology, and electrode thickness. Fig. 1a presents a scanning electron microscopy (SEM) image of a secondary polycrystalline particle composed of tens of thousands of primary single-crystal particles. The ion intercalation of these densely packed primary particles within the secondary structure can be modeled using either diffusion-limited or reaction-limited assumptions.

First, for a diffusion-limited picture depicted in Fig. 1b, we utilize a phase-field formulation [18] adapted to describe particle filling limited by solid-state transport within a secondary particle, governed by chemical potential. In addition, phase transitions are not confined solely to diffusion-limited secondary particles but also occur at the scale of a primary particle ensemble. These ensemble-scale phase transitions are driven by interfacial reactions [19,20], which are determined by chemical potential differences [21,22]. Second, a scaling law predicts that when the average particle size is below one micron and with applied current less than 100C for graphite, the system becomes reaction-limited [23]. Considering submicron-sized primary particles commonly found under typical operating conditions [15], we adopt a reaction-limited formulation [22,24] for primary particle intercalation, as illustrated in Fig. 1c. While diffusion-limited and reaction-limited pictures can co-exist and are observed in graphite electrodes under the same conditions [16], we consider both in our physics-based learning framework for modeling chemical potential.

Physics-based learning. Physics-based learning is a hybrid modeling approach that combines domain-specific knowledge from classical partial differential equation (PDE)-based systems with data-driven techniques [25]. This methodology has been previously utilized for model order reduction to accelerate battery model simulations [26]. To enable

the efficient learning of chemical potentials, we develop a new method to uncover hidden physics and address uncertainties by incorporating the Bayesian inference, leading to Bayesian model integrated neural networks (BMINN). The major innovation of BMINN is its capability to accurately infer chemical potentials from voltage data alone. This is particularly critical for multi-phase battery modeling, where precise chemical potential profiles are essential to capturing phase transition dynamics in graphite electrodes.

BMINN achieves this by parameterizing hidden physics using a flexible and stochastic function that can relate to any signal in a physics-based model, including time, differential states, algebraic states, control inputs, and spatial coordinates. Unlike methods such as the SINDy algorithm [27], BMINN does not impose predefined functional forms for unknown physics. Compared to inverse physics-informed neural networks (iPINNs) [28], which rely on learning specific solution trajectories in the inverse problem (*Supporting Information S8*), BMINN is designed to uncover hidden system dynamics while providing uncertainty quantification, as mentioned earlier. The hybrid framework combines known physics-based equations (non-autonomous PDEs and, where appropriate, partial differential–algebraic equations, PDAEs) with Bayesian neural networks to produce a data-driven function that accounts for both parameterization errors and modeling errors resulting from model mis-specifications. By enabling robust uncertainty quantification and physics-based insights, BMINN provides a versatile and generalizable tool for modeling electrochemical systems and, more broadly, multi-phase non-equilibrium dynamics.

2.2. Reconstructing electrode thermodynamics

BMINN enables direct reconstruction of Gibbs free energies (g) and chemical potentials (μ) as functions of the filling fraction x in Li_xC_6 from routine half-cell cycling data, with quantified uncertainties (*Supporting Information S1*). The inference is performed on current–voltage data collected during a C/40 charge–discharge cycle at 25 °C, which employs either a diffusion-limited or a reaction-limited formulation (*Supporting Information S2–S4*). Specifically, porous electrode theory (PET)-based chemical potentials take on a logarithmic form, while OCP-fitted chemical potentials are obtained from OCP measurements. In contrast, all other energies and potentials are inferred without imposing any predefined functional forms. This allows greater flexibility in capturing hidden physics. This flexibility is important, as modeling errors often arise from incorrect assumptions about functional dependencies. By avoiding such constraints, BMINN leverages the universal approximation capabilities of neural networks to uncover hidden physics and provide accurate, data-driven insights into multi-phase intercalation dynamics.

In addition to enabling flexible inference, it is important to assess the credibility of the inferred energies and potentials. Point estimates, such as maximum *a-posteriori* (MAP) or maximum likelihood estimation, often fail to account for the credibility or variability of the inferred parameters, which can be particularly problematic when dealing with limited and noisy data. In the absence of internal sensors, external and often noisy current–voltage data make a Bayesian formulation particularly suitable for this purpose. As shown in Fig. 2, posterior distributions of energies and potentials are sampled, revealing that they converge to unimodal distributions. Interestingly, the posterior distributions associated with the phase-field formulation exhibit a wider confidence interval (CI), which indicates a higher level of uncertainty compared to the reaction-limited formulation. This quantification of uncertainty provides valuable insights into factors such as data noise and the influence of the specific physics-based formulation used.

As shown in Fig. 2a, the Gibbs free energies learned with phase-field and reaction-limited formulations display four distinct energy wells at filling fractions of approximately 0.1, 0.2, 0.5, and 0.9. These energy wells correspond to Stages 3L, 2L, 2, and 1 of the lithiated graphite phases, respectively. Preceding Stage 3L, we designate XL to represent liquid-like structures that exhibit a periodicity beyond three layers. Compared to a multi-phase-field model [10], which only captures transitions between stable phases, both Gibbs free energy profiles derived from the two physics-based formulations exhibit energy minima associated with transient liquid-like (L) phases. Thermodynamically, the common tangents of the double-well energies at 3L–2L, 2L–2, and 2–1 coincide with the filling fractions where voltage plateaus are observed. Two of these tangents are illustrated for the maximum *a-posteriori* (MAP) Gibbs free energies in Fig. 2b.

The staging is clearly identifiable in chemical potentials μ, which represent the change in Gibbs free energies, as shown in Fig. 2c. The notation of the transient phases signifies different stacking structures beyond integer average numbers of graphene layers between lithium layers [29], as illustrated in Fig. 2d. Phase transitions occur between the extrema of the chemical potentials, where $d\mu/d\mathrm{x} = 0$. For the experimentally inaccessible concentration regions where x is close to 0 and 1, corresponding to fully de-lithiated and lithiated states, both the Gibbs free energy and chemical potential models become unreliable. However, the particle population adopting these concentrations is negligible, as the cutoff voltages typically prevent the average capacity from reaching these regions. In practice, these regions can be extrapolated using logarithmic functions so that μ approaches $-\infty$ at $\mathrm{x} = 0$ and ∞ at $\mathrm{x} = 1$ [30], although it may introduce instabilities in the numerical schemes of physics-based simulations. Moreover, the energies and potentials learned using the two physics-based formulations are consistent in their overall shapes but show slight differences in numerical values. For example, the chemical potential learned using a phase-field formulation during a Stage 2–1 transition is lower compared to the chemical potential learned using a reaction-limited formulation. This is expected since the two physics-based formulations are based on different predefined mathematical structures, even though they are trained on the same dataset.

In comparison, OCP-fitted energy and potential curves commonly used in existing electrode-specific phase-field formulations [31–33], as plotted in Fig. 2a and c capture the general trend, but many features are missing. The OCP-fitted chemical potential is derived using the Nernst relation $\mu = e_0(\phi_{\mathrm{OCP}} - \phi_{\mathrm{ref}})$, where e_0 is the elemental charge, ϕ_{OCP} represents a fitting function of OCP, and ϕ_{ref} is a reference potential taken as the voltage of the first major plateau. As shown in Fig. 2c, the OCP-fitted chemical potential is a monotonic function in which, within the plateau regions, some distinct stages (e.g., XL, 3L, and 2L) are ambiguous to identify. For the OCP-fitted Gibbs free energy in Fig. 2a, the energy barriers are absent, which is not thermodynamically consistent with phase transitions occurring in graphite electrodes. Similarly, classical intercalation models, such as Newman's model based on porous electrode theory [34], assume a chemical potential of the form $\mu = k_B T \ln \mathrm{x}$ where k_B and T are the Boltzmann constant and temperature. A monotonic chemical potential does not result in phase coexistence and energy barriers in the Gibbs free energy. These energy barriers not only display plateaus (through common tangent construction) in equilibrium but also play an important role in the intercalation dynamics. It was observed in an *operando* XRD study [1] that lithiation ceases in regions where Stage 2 is reached during charge. In kinetic simulations of realistic graphite electrodes, it is crucial to take into account the energy barriers so that regions undergoing transitions associated with smaller energy barriers draw higher current rates, consistent with experimental observations.

2.3. Capturing phase transitions and XRD signatures

The reconstructed Gibbs free energies not only reproduce graphite's staging transitions in population dynamics but also match operando XRD signatures. To demonstrate the importance of a thermodynamically consistent description of Gibbs free energy in graphite intercalation dynamics, we compare different free energy models. In Fig. 3a, the evolution of population densities resulting from the reaction-limited

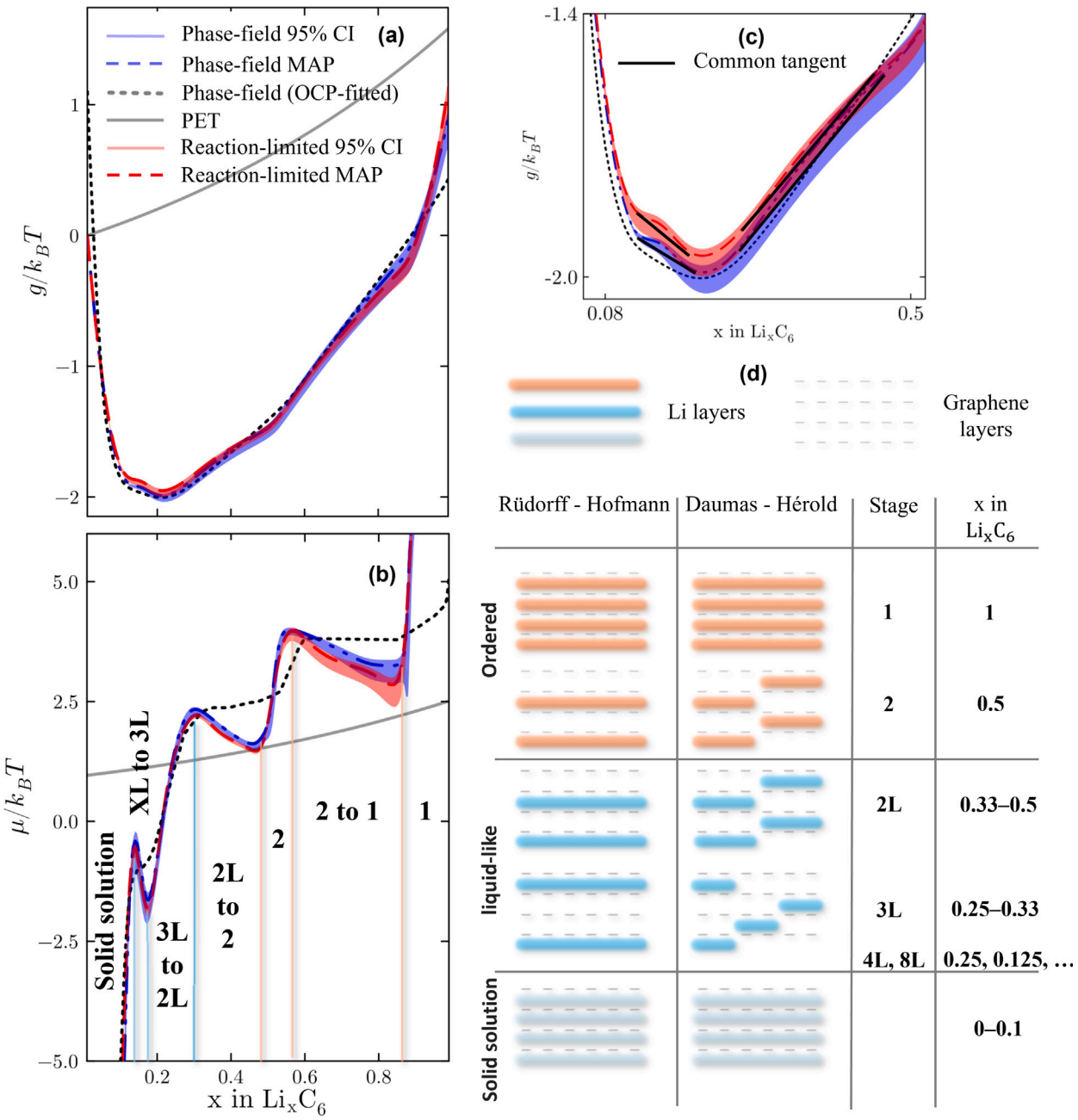

Fig. 2. (a) Gibbs free energies. (b) Two common tangents (black solid lines) of the maximum *a-posteriori* value (dashed line) of the Gibbs free energies for the 3L–2L and 2L–2 transitions. (c) Chemical potentials. All the energies and potentials are scaled to thermal energy k_BT, and are sampled from the posterior distributions obtained from a C/40 charge–discharge cycle. The intensity of the color is proportional to the probability density of the posterior distribution. (d) The staging structures of different stages, including dense stages where the lithium ions are intercalated on interstitial sites and liquid-like stages where graphene layers are filled without particular in-plane order. Disordered lithium ordering with lithium content lower than 3L, e.g. Stage 4L and 8L, are denoted by XL.

Gibbs free energy model undergoing a C/20 charge–discharge cycle is plotted. The simulation starts with an equilibrium, unimodal distribution at a low state of charge (SOC) value at the beginning of charge. Subsequently, it undergoes three major phase transitions, i.e. XL–3L, 3L–2, and 2–1, each characterized by their corresponding bimodal distributions. Throughout these phase transitions, one peak expands and grows at the expense of the other; for instance, the Stage 1 peak grows while the Stage 2 peak diminishes during the 2–1 transition. The discharge distributions follow a similar mechanism, capturing all phase transitions, but they are not exact reversals of the charge distributions over time due to the combined effects of hysteresis and polarization. In contrast, the population densities resulting from the PET-based model exhibit an advection of a unimodal distribution throughout charge and discharge. As shown in Fig. 3b, there is no expansion, split, or growth of the peak observed. Moreover, no discrepancies between charge and discharge arise from the hysteretic effect, which is not consistent with graphite [5,35]. It can be concluded that although classical intercalation models may reproduce the voltage behavior of a graphite electrode, they do not accurately model the internal states.

Experimental *in situ* and *operando* techniques probing the internal states of a battery include XRD [1,2], neutron diffraction [36], and optical microscopy [16,32]. These methods typically involve unrealistic *operando* cell designs or costly experiments, making them infeasible for periodic assessments of commercial battery cells in the field. However, it is well-known that degradation processes, such as lithium plating, are closely coupled with graphite internal states [37]. Therefore, an

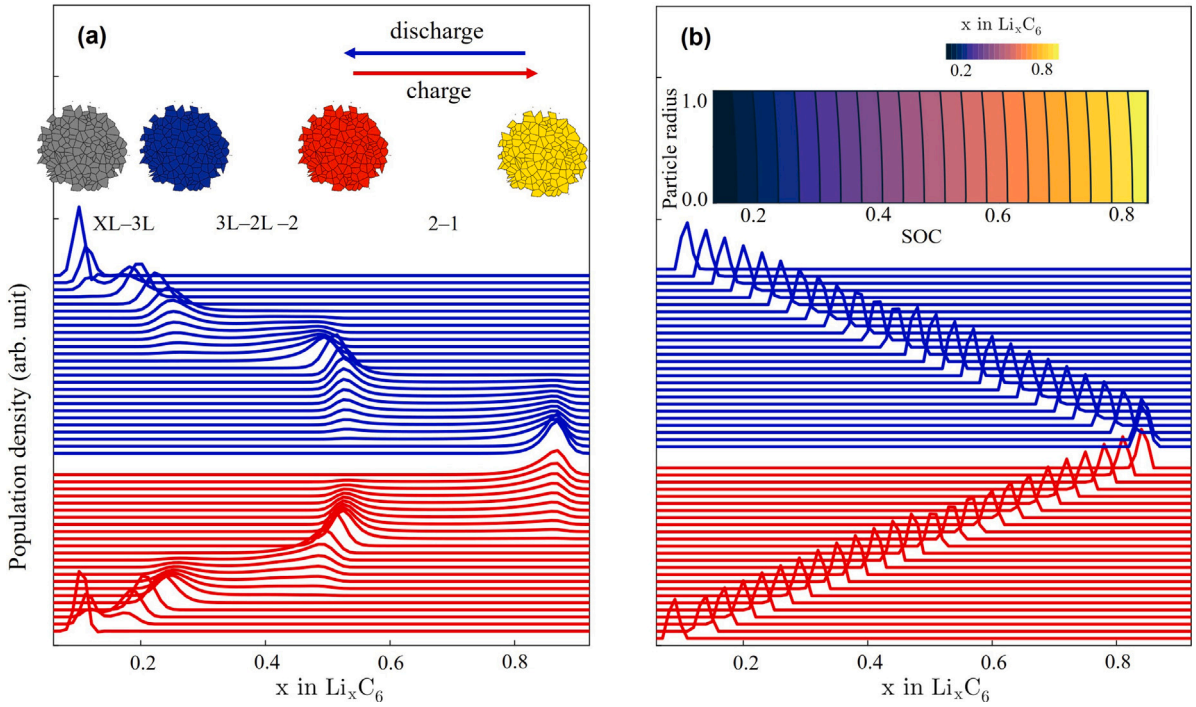

Fig. 3. Population densities during a C/20 charge (red) and discharge (blue) cycle resulting from (a) the reaction-limited Gibbs free energy model and (b) the PET-based Gibbs free energy model. Since graphite is a chromogenic material, the color of the particles in the inset of (a) corresponds to those observed in optical experiments [16]. The inset in (b) shows a spatiotemporal plot of the filling fraction for a single (volume-averaged) secondary particle. The population densities for the PET-based model are computed from the spatio-temporal profile of the filling fraction (see *Supporting Information*).

accurate model for the internal states of graphite electrodes is highly desirable. To validate different models, the XRD patterns resulting from each model are computed (*Supporting Information*). Fig. 4a shows an *operando* XRD measurement of a graphite electrode undergoing a C/20 charge at 25 °C [2]. The simulated contour plots of changes in the 2θ angle and intensity of graphite basal reflections for various models are shown in the same figure. It can be seen that the simulated *operando* XRD resulting from the phase-field and reaction-limited free energy models closely resemble the overall pattern of experimental measurements, as shown in Fig. 4b and c, respectively. From a physics perspective, the agreement indicates that the learned free-energy functional reproduces the equilibrium common-tangent structure and the rate-dependent sequence of staging transitions observed by *operando* XRD, providing a direct bridge between phase diagrams and driven intercalation trajectories.

The PET-based free energy model in Fig. 4d produces a solid-solution pattern throughout the charge, which differs significantly from the experiment. This is a direct consequence of the fact that PET-based chemical potential is monotonic by construction (Eqn. 2b in the *Supporting Information*), implying a convex free-energy landscape that cannot reproduce phase coexistence or energy barrier-controlled transitions. Fig. 4e and f show the results of OCP-fitted free energy models in combination with the phase-field and reaction-limited formulations, respectively. These models exhibit solid-solution-like behavior from the start of charging to Stage 2, located at around 25.2° in 2θ, differing from the phase separation patterns resulting from our free energy models in Fig. 4b and c and the experiment. Furthermore, the Stage 2–1 transition for the OCP-fitted models, which should initiate at around 50% SOC, is significantly delayed and behaves like a solid solution from 50% to 65% SOC. These behaviors are inconsistent with the experimentally measured XRD pattern.

The above results clearly reveal how important an accurate and realistic description of the Gibbs free energy is in modeling the internal intercalation dynamics of graphite electrodes. Even though the PET-based and OCP-fitted models successfully reproduce current–voltage behaviors of graphite electrodes through system identification [38,39], the accuracy of these models in the internal states can be erroneous. Our models, based on physics-based Bayesian learning, prescribe accurate Gibbs free energies with realistic energy barriers and chemical potentials. The energy barriers are crucial in the heterogeneous lithiation of graphite under fast-charging conditions. Larger energy barriers inhibit local intercalations and transport, causing the lithiation front to move and "shoulders" or stagnations in the filling fractions to form [1]. Such energy-barrier-related phenomena have been observed experimentally using *operando* XRD [1,40], yet remain elusive in current modeling efforts.

The internal states of graphite are closely coupled with reaction kinetics and ionic transport, which together significantly influence its intercalation dynamics. Many degradation mechanisms in graphite draw side reaction currents from the intercalation currents, meaning they are also affected by these internal states. One unexpected feature observed during the heterogeneous delithiation of graphite is the increase in Stage 1 population at the end of a constant voltage discharge [1,40]. Since this phenomenon occurs only in specific stages, it is of great value to quantify the contribution of each stage, specifically the mass fractions associated with them. Traditionally, decoupling the contributions of different stages is typically achieved through Rietveld refinement and integration of the XRD peaks. However, this technique can lead to ambiguous interpretations because XRD patterns may be obscured by peaks from the cathode, current collector, or casing. Additionally, some phases are challenging to decouple due to weak reflection splitting of Bragg peaks [41]. In this context, our Gibbs energy models, combined with a suitable physics-based formulation, can help accurately quantify the dynamics of phase populations, thereby enhancing the predictive capability of both simulations and experiments.

The applications of realistic Gibbs free energy models featuring accurate energy barriers are essential for advancing the understanding and prediction of graphite internal intercalation dynamics. First, XRD simulations based on these models facilitate quantitative degradation

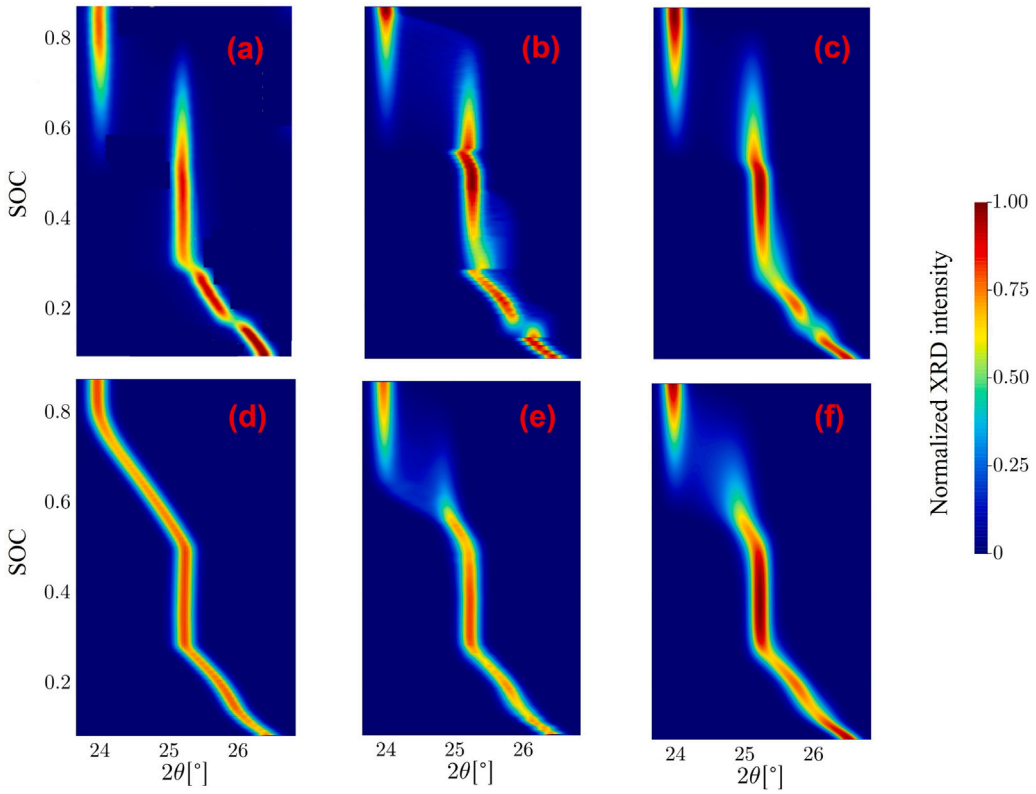

Fig. 4. Contour plot of changes in the 2θ angle and intensity of graphite basal reflections for a graphite electrode undergoing a C/20 charge at 25 °C. (a) *Operando* XRD measurement [2]. (b) Simulated XRD using the phase-field Gibbs free energy model. The numerical results at certain SOCs may not be reliable due to large chemical potential gradients and sharp phase boundaries. (c) Simulated XRD using the reaction-limited Gibbs free energy model. (d) Simulated XRD using the PET-based free energy model. (e) Simulated XRD using an OCP-fitted Gibbs free energy model with the phase-field formulation. (f) Simulated XRD using an OCP-fitted Gibbs free energy model with the reaction-limited formulation.

modeling, which is key for developing health-conscious control strategies in battery management systems. For instance, accurately predicting the formation of LiC_6 phase in graphite is critical for optimizing fast charging protocols to limit lithium plating. Second, model-assisted Rietveld refinement, leveraging the detailed energy barrier information, can be used to interpret experimental XRD results more effectively. This approach can help decouple complex phase contributions that might be challenging in experimental data, leading to a more reliable analysis of the internal states and dynamics within the battery.

2.4. Generalization to device-scale models

Finally, we demonstrate that the framework generalizes to commercial battery cells, where it enables faithful voltage prediction and internal state estimation. In such cells, three-electrode experiments can be performed to characterize individual electrodes, as detailed in *Supporting Information* S1. In commercial-format cells, unlike in coin cells, the lithium-ion concentration in the electrolyte and the intercalation rate at the particle surface can generally be treated as uniform along the in-plane direction, owing to the large aspect ratio and effective current collection. Under low current conditions, these quantities can also be considered uniform across the electrode thickness (out-of-plane) dimension (see *Supporting Information* S4.1). This simplification allows chemical potentials to be inferred without coupling electrolyte dynamics in the thickness dimension to intercalation dynamics, which would otherwise introduce additional PDEs and algebraic constraints. However, when currents exceed the limits of the single-particle assumption, electrolyte dynamics and spatially distributed intercalation rates must be incorporated for accurate modeling and predictions for downstream model-based applications.

To demonstrate the effectiveness of our approach in downstream applications, such as terminal voltage prediction, the inferred chemical potential is integrated into a full-cell model. This model uses a phase-field formulation for ion concentration in the solid phase, coupled with distributed ion concentration in the electrolyte and distributed intercalation rates, as previously formulated by Huang et al. [26]. The parameterization is based on an LG™ M50 cylindrical cell [38]. Parameter identification for the electrolyte-related parameters is performed using C/2 constant-current discharge data of a pristine cell at 25 °Celsius. Model validation is carried out using hybrid pulse power characterization (HPPC) and galvanostatic intermittent titration technique (GITT) profiles, which are widely used for evaluating battery performance and relaxation dynamics.

Fig. 5a shows the voltage prediction of the fitted full-cell model under an HPPC-type current profile, where the inset depicts the current profile used during testing. The prediction closely tracks the experimental data, achieving a root-mean-square error (RMSE) of 14.7 mV. In Fig. 5b, the voltage prediction for a GITT-type profile is shown to effectively capture the transient behavior of the voltage relaxation but exhibits a small steady-state error for certain GITT pulses. This highlights a persistent challenge in parameterizing full-cell electrochemical models, especially for pulsing and dynamic current profiles. We emphasize that, while many battery models with differing physical assumptions can achieve reasonable accuracy in terminal voltage prediction, faithful internal state estimation remains a significant advantage of more physically detailed models. Such insights are vital for applications like battery diagnostics and health-aware control, where internal states are more informative than voltage alone.

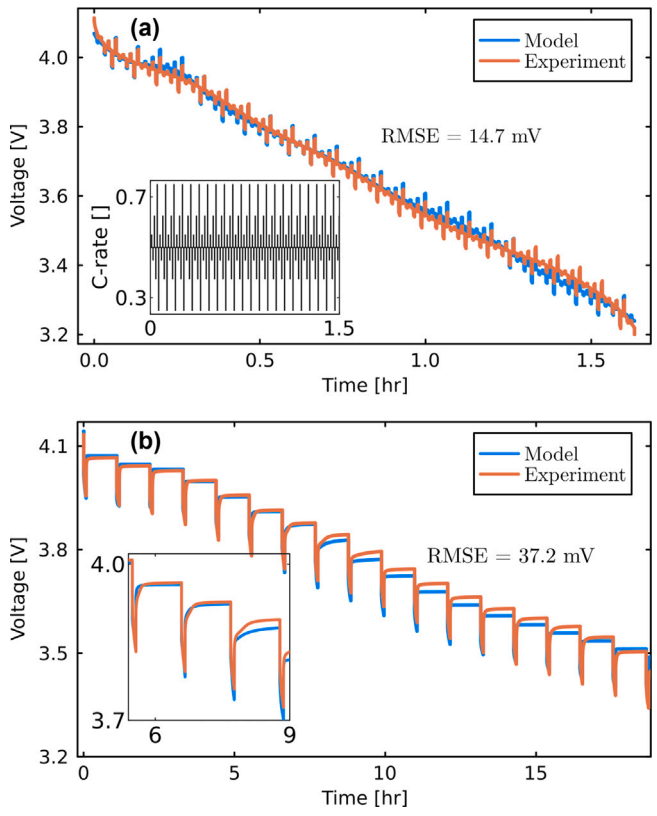

Fig. 5. Testing of a full-cell model using two current profiles cooled at 25 °C. (a) Voltage prediction under an HPPC-type profile, with the inset showing the corresponding current profile. (b) Voltage prediction for a GITT profile, with the inset displaying an enlarged view of relaxation behavior on the voltage curve.

3. Theory

3.1. Physics-based learning of hidden physics and uncertainties

Physics-based electrochemical models, typically formulated as PDEs or partial-differential algebraic equations (PDAEs), face significant challenges when applied to real-world energy storage systems. These challenges arise from two main factors. First, the high-dimensional parameter space inherent in these models complicates parameter identification, particularly when using Bayesian estimation techniques. Over-parameterization exacerbates this issue, leading to poor inferability, predictability, and generalizability due to the increased prediction uncertainty caused by fitting numerous free parameters. Second, all models are subject to modeling errors as a result of changed operating conditions, parameter variability, and simplifications made during model development. These errors are often introduced by misspecifications in the dynamic system, which can result from unphysical assumptions or oversimplifications during model order reduction.

A major source of modeling errors arises from hidden physics that remain latent and unaccounted for in the model specification. BMINN is specifically designed to handle these errors while accounting for uncertainties in general dynamic systems. The architecture and key concepts of BMINN are illustrated in Fig. 6. This hybrid approach ensures fidelity to physical laws while leveraging the approximation capacity of neural networks and quantifying uncertainties given the available, potentially noisy data or incomplete data.

The interpretability of BMINN is attributed to its hybrid architecture, where known physics-based equations constrain the learning process and hidden states correspond to electrochemical states of a battery. The unknown components (Fig. 6d) characterizing the hidden physics, are explicitly parameterized and inferred. Furthermore, the Bayesian component of BMINN provides posterior distributions for learned parameters, offering a probabilistic measure of uncertainty. This uncertainty accounts for data noise, sparsity, and model mis-specification, making it a critical indicator of the reliability and robustness of predictions.

BMINN targets a class of non-autonomous PDAE-based systems described by

$$\frac{\partial H_d}{\partial t} = F\left(t, H_d, H_z, \Phi(\cdot), u\right), \tag{1a}$$

$$0 = G\left(t, H_d, H_z, \Phi(\cdot), u\right), \tag{1b}$$

$$y = Y\left(t, H_d, H_z, \Phi(\cdot), u\right), \tag{1c}$$

where t is time, u denotes the external control input that makes the system non-autonomous, y is the measurable system output, and F, G, and Y are functions. H_d and H_z represent differential states and algebraic variables, respectively. All the states and algebraic variables are time-dependent and spatially distributed, in which the spatio-temporal coordinates, i.e., t and $\mathbf{x}$, are ignored for brevity. $\Phi(\cdot)$ is an unspecific function that can be dependent on t, $\mathbf{x}$, H_z H_d, or u., and it is included in the model formulation to cover any possible hidden physics and uncertainties. The identification of $\Phi(\cdot)$ will be affected by the employed labeled input–output dataset, denoted by D. By leveraging Bayesian principles to model uncertainty in data, Bayesian machine learning can be a powerful tool to identify $\Phi(\cdot)$. Because of modular and flexible design, recurrent neural networks (RNN) are particularly suited for sequence-to-sequence applications, while as a bi-directional network, residual neural networks (ResNets) can model dynamic systems with time-stepping of states governed by the system dynamics and control input. Integrating these different neural networks may enable highly efficient learning for the dynamics of complicated systems that are nonlinear, non-autonomous, and singularly perturbed. Following this thread, we propose to approximate $\Phi(\cdot)$ by Bayesian neural network (BNN), Φ_{BNN}, parameterized by p_θ, leading to

$$\Phi(\cdot) = \Phi_{\text{BNN}}\left(t, \mathbf{x}, H_d, H_z, u; p_\theta\right), \tag{2}$$

where p_θ stands for the distribution of parameters θ, namely $p_\theta = p(\theta)$, and θ includes both battery physical parameters and the BNN's parameters. Consequently, the formulation of BMINN can be given by

$$\frac{\partial H_d}{\partial t} = F\left(t, H_d, H_z, \Phi_{\text{BNN}}, u\right), \tag{3a}$$

$$0 = G\left(t, H_d, H_z, \Phi_{\text{BNN}}, u\right), \tag{3b}$$

$$y = Y\left(t, H_d, H_z, \Phi_{\text{BNN}}, u\right). \tag{3c}$$

Note that the model formulation obtained above for BMINN blends the physics-based part captured by functions F, G, and Y, and the data-driven part, i.e., Φ_{BNN} within each of these functions.

By appropriately discretizing (3) in both the spatial and time domains, we can obtain BMINN in the discrete form

$$h_d^{k+1} = f\left(k, \delta t^k, h_d^k, h_z^k, \Phi_{\text{BNN}}^k, u^k\right), \tag{4a}$$

$$0 = g\left(k, h_d^k, h_z^k, \Phi_{\text{BNN}}^k, u^k\right), \tag{4b}$$

$$y^k = y\left(k, h_d^k, h_z^k, \Phi_{\text{BNN}}^k, u^k\right), \tag{4c}$$

where k is the discrete-time index. δt^k is the step size at time step k that can be controlled by an adaptive time integrator. h_d and h_z are the spatially discretized differential states and algebraic variables, respectively, and $\Phi_{\text{BNN}}^k = \Phi_{\text{BNN}}(k, \mathbf{x}, h_d^k, h_z^k, u^k; p_\theta)$. The form of the function $f(\cdot)$ is dependent on the time integration scheme, which can take the arguments h_d^{k+1} and h_z^{k+1} if an implicit scheme is used. Φ_{BNN}^k can be parameterized by BNN with a set of parameters and hyper-parameters to optimize.

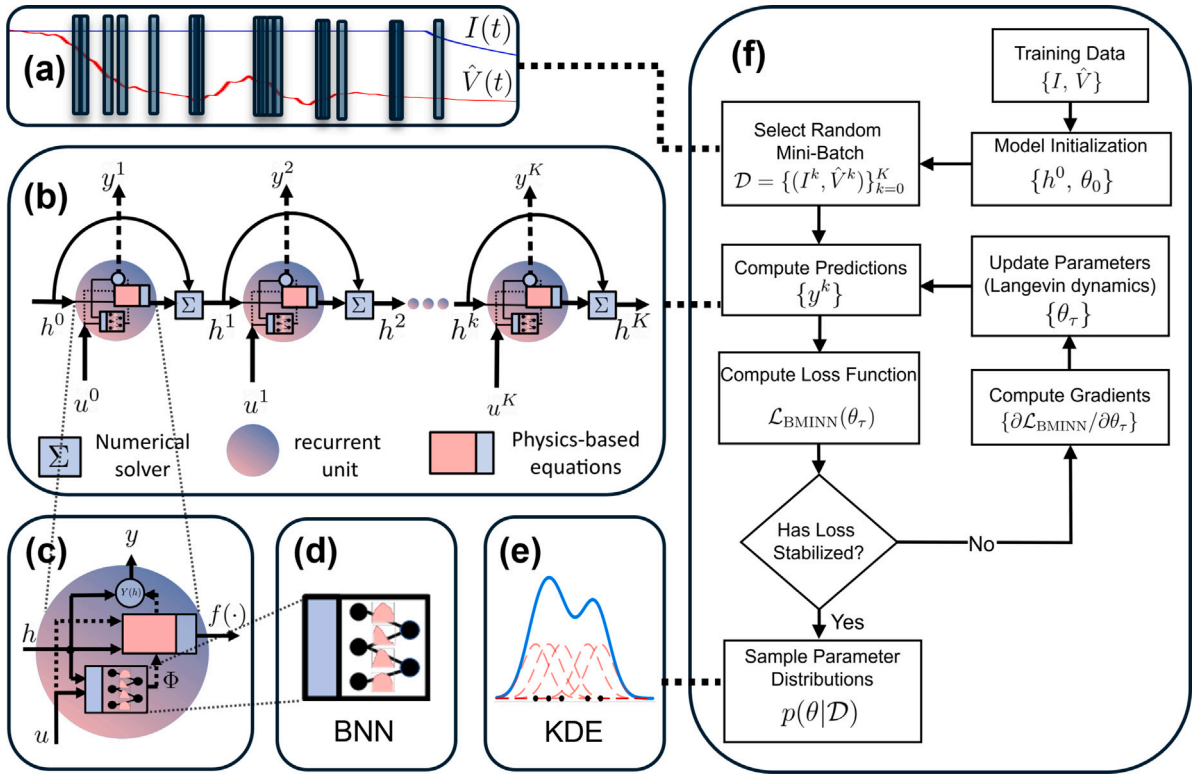

Fig. 6. The architecture and key concepts of BMINN for learning hidden physics and quantifying uncertainties in dynamic systems. (a) Data batching illustrated for battery training data, consisting of a two-dimensional vector of K randomly selected points from current and voltage time-series data. (b) The iterative update process of hidden states h^k, input u^k, and output y^k in the BMINN architecture. (c) The design of the physics-based recurrent unit, incorporating physics-based equations, Bayesian neural networks (BNN), an output function $y = Y(h)$, and an unknown function Φ representing the hidden physics. (d) Quantification of uncertainties by learning the distributions of weights and biases in BNN. (e) Sampling of the posterior distribution using kernel density estimation (KDE). (f) Flowchart of the BMINN training algorithm illustrated for a battery system.

The distribution p_θ of the parameters θ is learned by evaluating the loss function $\mathcal{L}_{\text{BMINN}}$ for multiple parameter sets sampled from p_θ

$$\mathcal{L}_{\text{BMINN}}(\theta) = \frac{1}{K}\sum_{k=0}^{K}\left[y\left(k, h_d^k, h_z^k, \Phi_{\text{BNN}}^k, u^k\right) - \hat{y}^k\right]^2 \delta t^k, \quad \text{s.t. (4a)–(4b)}, \tag{5}$$

where K denotes the total number of labeled input–output pairs, i.e. $\mathcal{D} = \{[u^1, \hat{y}^1], \ldots, [u^k, \hat{y}^k], \ldots, [u^K, \hat{y}^K]\}$, and $\hat{y}^k$ is the measured system output. If the value of $\mathcal{L}_{\text{BMINN}}$ for a sampled model is small, it implies that the parameter values produce model outputs closely matching the observed data. This means the loss function defined above for a sampled parameter set is inversely proportional to the likelihood of $\mathcal{D}$ for a given θ, denoted by $p(\mathcal{D}|\theta)$. Specifically, the relationship between the loss function and the log-likelihood $\log p(\mathcal{D}|\theta)$ is given by:

$$\mathcal{L}_{\text{BMINN}}(\theta) \propto -\log p(\mathcal{D}|\theta). \tag{6}$$

The training procedure is illustrated in Fig. 6f. Given some randomly selected mini-batch of measured input–output pairs and an initial condition for the hidden states, we unroll the physics-based recurrent unit forward in time using the chosen time integrator to obtain predictions $\{y^k\}$ and the corresponding hidden states. We then minimize the mean-squared voltage mismatch $\mathcal{L}_{\text{BMINN}} = \frac{1}{K}\sum_k (y^k - \hat{y}^k)^2$ subject to the constraints (4a)–(4b). These constraints are not included in the loss function as soft residual penalties at collocation points, but are instead enforced as hard constraints by the time integrator within the physics-based recurrent unit, which avoids ill-conditioned residual balancing and is therefore not prone to the gradient pathologies commonly observed in soft-constrained PINN training. Lastly, the gradients with respect to both physical parameters and BNN parameters are obtained by differentiating through the solver. For uncertainty quantification, we sample from the posterior using SGLD (10) and MAP estimation is recovered by using the posterior mode.

3.1.1. Uncertainty quantification

The BNN, Φ_{BNN}^k, in the general problem formulation of BMINN can be realized by a deep stochastic neural network consisting of an input layer $\mathbf{a}^{[1]}$, a succession of L layers, and an output layer polluted by random noise ϵ. This neural network can be generally formulated as

$$\begin{cases} \mathbf{a}^{[1]} = [k, \mathbf{x}, h_d^k, h_z^k, u^k]^T, \\ \mathbf{a}^{[l]} = \sigma\left(\mathbf{W}^l\,\mathbf{a}^{[l-1]} + \mathbf{b}^l\right), \quad \text{for} \quad l = 2, 3, \ldots, L, \\ \Phi_{\text{BNN}}^k = \mathbf{W}^L\mathbf{a}^{[L]} + \mathbf{b}^L + \epsilon^k, \end{cases} \tag{7}$$

where $\sigma(\cdot)$ is the activation function. For layer l, $\mathbf{W}^l$, $\mathbf{b}^l$, and $\mathbf{a}^{[l]}$ represent the weight matrices, biases, and activation.

The parameters θ embedded in Φ_{BNN} are considered random variables for which the entire distribution is estimated from $\mathcal{D}$. Given a prior distribution of parameters $p(\theta)$, by Bayes' theorem, the posterior distribution $p(\theta|\mathcal{D})$ is proportional to the product between the prior and the likelihood of the dataset given the parameter $p(\mathcal{D}|\theta) = \Pi_1^K p([u^k, \hat{y}^k]|\theta)$, i.e.,

$$p(\theta|\mathcal{D}) \propto p(\theta)p(\mathcal{D}|\theta). \tag{8}$$

The most probable parameter set of θ, defined as $\theta_{\max}$, in a MAP estimation, maximizes the posterior distribution. This is done by taking the logarithm of posterior in (8), leading to the maximization problem

$$\theta_{\max} = \arg\max_\theta \left[\log p(\mathcal{D}|\theta) + \log p(\theta)\right]. \tag{9}$$

To take advantage of the full posterior distribution, one has to evaluate multi-dimensional integrals, such as the posterior expectation and variance with respect to parameters θ, or to sample from the posterior using

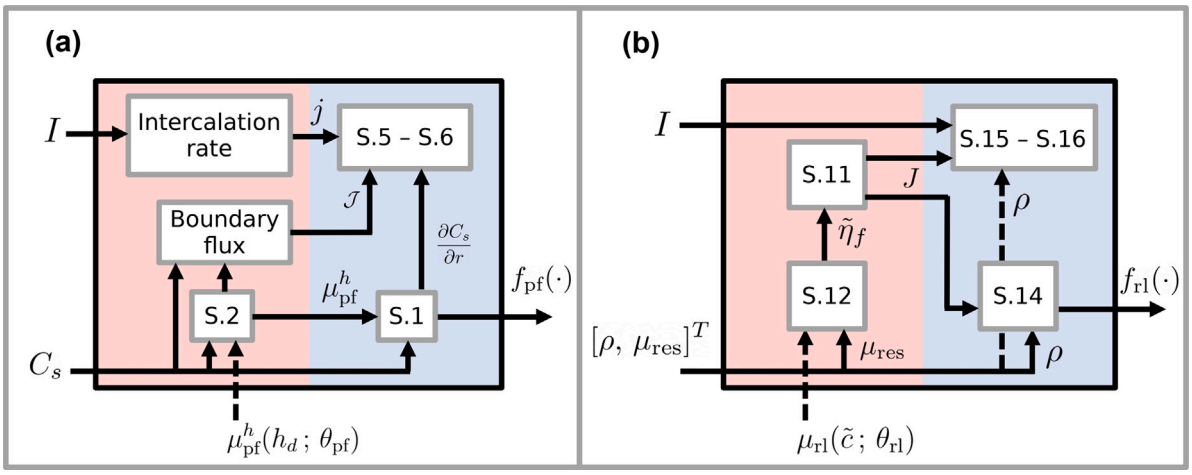

Fig. 7. The physics-based recurrent unit design in BMINN for learning missing physics parameterized by u^h_{pf} and u_{rl}. (a) The recurrent unit within BMINN realized for the phase-field model with the hidden state $h_d = C_s$ and control input $u = I$. (b) The recurrent unit realized for the reaction-limited model with hidden state $[h_d,\ h_z]^T = [\rho,\ \mu_{\rm res}]^T$ and control input $u = I$. The equations S.1–S.16 in the figure correspond to physics-based formulations laid out in *Supporting Information* S2–S3.

Markov chain Monte Carlo. However, this generally does not scale well with the number of parameters involved in physics-based machine learning. To avoid this, we adopt the stochastic gradient Langevin dynamics (SGLD) [42], which stochastically updates the parameters according to the Langevin stochastic differential equation:

$$\theta_{\tau+1} = \theta_\tau + \frac{\epsilon_\tau}{2}\left(-\frac{\partial \mathcal{L}_{\rm BMINN}(\theta_\tau)}{\partial \theta_\tau} + \frac{\partial \log p(\theta_\tau)}{\partial \theta_\tau}\right) + \Gamma_\tau,\ \text{where}\ \Gamma_\tau \sim \mathcal{N}(0, \epsilon_\tau) \tag{10}$$

where τ is the iteration index, ϵ_τ is a positive parameter denoting the learning rate, and Γ_τ is a normally distributed random variable in the Langevin dynamics to ensure that the parameter trajectory converges to a full posterior distribution. The loss term $\mathcal{L}_{\rm BMINN}(\theta_\tau)$ defined in (5) is equivalent to the negative log-likelihood function due to (6). $\partial \log p(\theta_\tau)/\partial\theta_\tau$ serves as a regularization term in the above update law for parameters θ.

3.2. Learning chemical potentials

The BMINN framework facilitates accurate identification of hidden physics within PDE- or PDAE-based models, specified in *Supporting Information* S2–S4, along with their associated physical parameters. To learn material-specific chemical potentials in these physics-based formulations, we first acknowledge that the battery data consists of externally measurable quantities, such as the applied current I and voltage V, as well as internal states, such as the lithium-ion concentrations. While I and V can be readily obtained in a three-electrode setup, the internal states of electrodes must be estimated using advanced spectroscopy techniques. Among these, *operando* XRD spectroscopy has proven effective for capturing internal states under battery operational conditions [1]. However, such methods require access to high-energy synchrotrons and specialized cell designs. Furthermore, the X-ray or neutron exposure involved in these techniques can inadvertently alter the system states, including the electrode potential and temperature [43], thereby impacting the reliability of the data for learning chemical potentials.

To infer chemical potentials from externally measured current–voltage data using BMINN, we design two physics-based recurrent units corresponding to the phase-field and reaction-limited models, as illustrated in Fig. 7. For the dynamic electrochemical system of graphite electrodes, the hidden states, h_d, represent lithium-ion concentrations in active materials, C_s, in the phase-field model, while in the reaction-limited model, the hidden states are $[h_d,\ h_z]^T = [\rho,\ \mu_{\rm res}]^T$, where ρ and $\mu_{\rm res}$ denote the population density and reservoir chemical potential, respectively. After spatial discretization, the dynamic part of the PDE system (S.1)–(S.7) and the PDAE system (S.11)–(S.16) in the *Supporting Information* are expressed in the following forms

$$\frac{dh_d}{dt} = f_{\rm pf}\left(h_d,\ \mu^h_{\rm pf}(h_d\,;\,\theta_{\rm pf}),\ I(t)\right) \quad \text{(phase-field model);} \tag{11}$$

$$\frac{dh_d}{dt} = f_{\rm rl}\left(h_d,\ \mu_{\rm rl}(\tilde{c}\,;\,\theta_{\rm rl}),\ h_z,\ I(t)\right) \quad \text{(reaction-limited model),} \tag{12}$$

$$0 = g_{\rm rl}\left(h_d,\ \mu_{\rm rl}(\tilde{c}\,;\,\theta_{\rm rl}),\ h_z,\ I(t)\right) \quad \text{(reaction-limited model);} \tag{13}$$

Here, the system input is the applied current. The nonlinear functions $f_{\rm pf}$, $f_{\rm rl}$ and $g_{\rm rl}$ describe the system dynamics, and the chemical potentials, $\mu^h_{\rm pf}$ and $\mu_{\rm rl}$, associated with the phase-field and reaction-limited models, respectively, are learned alongside their physical parameters, $\theta_{\rm pf}$ and $\theta_{\rm rl}$, during the training of BMINN. The nonlinear functions $f_{\rm pf}$ and $f_{\rm rl}$ correspond to the general function $f(\cdot)$ in (4a) and in the recurrent units shown in Fig. 6c, representing the phase-field and reaction-limited cases, respectively. For PDAE formulations, the constraint $g_{\rm rl} = 0$ is enforced by employing a DAE solver. To fully implement BMINN for the battery system, the loss function (5) is established with multiple parameter sets sampled from the distribution of θ_m, where $m \in \{\text{pf}, \text{rl}, \text{pet}\}$ represents the model indices for phase-field, reaction-limited, and PET-based models, respectively. The loss function for each model $\mathcal{L}_{\rm BMINN}(\theta_m)$ is in the form

$$\mathcal{L}_{\rm BMINN}(\theta_m) = \frac{1}{K}\sum_{k=0}^{K}\left(V_m^k - \hat{V}^k\right)^2, \tag{14}$$

where the battery dataset $\mathcal{D} = \{(I^k, \hat{V}^k)\}_{k=0}^K$ consists of measured system outputs $\hat{V}^k$ and simulated outputs V_m^k, and K denotes the number of samples in the randomly selected mini-batch. This loss function is subject to constraints imposed by the electrode dynamics, as defined in Eqs. (11)–(13). The implementation to derive θ_m follows the Langevin stochastic differential Eq. (10), which provides uncertainty quantification for the learned parameters.

4. Discussion and outlook

Characterization of degradation. Fast charging is fundamentally constrained by degradation processes [44–46]. From a thermodynamic perspective, aging manifests as a gradual drift of the free-energy landscape: phase boundaries shift, metastable minima evolve, and energy barriers are reshaped. These changes alter the effective SOC ranges accessible to each electrode, features that are directly linked to degradation

modes [47] and can serve as markers for lifetime prognostics [48]. Conventional aging-adaptive approaches, which calibrate stoichiometry parameters from pseudo open-circuit voltage (OCV) curves, are limited by their reliance on predefined OCP functions. The error is particularly severe at the end of discharge, where the voltage is dominated by the graphite anode potential at low capacity. As a result, inaccurate identification of stoichiometry parameters penalizes any downstream battery model.

BMINN-based models offer a more fundamental route. By reconstructing material-specific Gibbs free energies directly from cycling data, they capture the reshaping of thermodynamic landscapes that underlies degradation. In practice, this reshaping is observed as the smearing of voltage plateaus and the broadening of transitions between adjacent stages, signatures that reflect side reactions and uneven participation of particle populations. Existing methodologies, which focus on terminal voltage alone, cannot resolve these effects because they lack accurate internal-state estimation. By contrast, BMINN quantifies how free-energy barriers evolve with cycling, linking macroscopic voltage drift to microscopic population dynamics. This physics-based description provides a coherent foundation for diagnosing degradation mechanisms and anticipating fast-charging failure modes such as lithium plating.

Modeling electrochemical impedance. The electrochemical impedance of a battery is highly sensitive to the equilibrium behavior of its half cells. This is because the reaction kinetics are calculated from the overpotential, which in turn depends on accurate estimation of the electrode's equilibrium surface concentration. Other than the fitted OCP functions, a widely adopted method in modeling electrochemical impedance is the multi-site multi-reaction (MSMR) theory [30], which breaks the OCP curve up into regions of solid-solution slopes and two-phase plateaus. It assumes the Nernst relation within the sloping regions and constant potential in the plateau regions. However, MSMR models are parameterized using pseudo-OCP measurements that deviate from true equilibrium due to polarization and hysteresis effects [35]. Within the BMINN framework, electrode potentials are learned directly from time-domain current–voltage trajectories, yielding thermodynamically consistent descriptors without requiring equilibrium measurements. The reaction-limited formulation captures both resistance polarization and low-current hysteresis [5]. More broadly, this shows how free-energy landscapes inferred from non-equilibrium driving can be used to reconstruct response functions, which is applicable beyond batteries wherever impedance or susceptibility encodes hidden thermodynamics.

Mechanical models. Pressure changes during cycling of graphite-based battery cells are dominated by negative-electrode expansion and contraction. External sensors can measure the resulting pressure or displacement, reflecting the total dilation of polycrystalline particle ensembles. However, these signals capture only bulk volume change and not the composition of phase-specific transitions, which limits their ability to resolve dynamic internal processes. In diagnostics such as lithium plating detection, abnormal pressure fluctuations have been correlated with *post-mortem* optical evidence of plating [49]. For graphite, plating often occurs during the Stage 2-to-Stage 1 transition, when a fraction of particles shifts from "half full" to "full", prompting the reduction of lithium ions to metallic lithium. The developed BMINN-based models provide a precise means of quantifying the population involved in the Stage 2–1 transition. In doing so, they separate thermodynamic contributions from bulk mechanical response, which suggests a general route to deconvolve hidden order-parameter dynamics from macroscopic signals in other materials where structural transformations couple to stress, strain, or volume change.

5. Conclusion

Learning hidden physics and unknown parameters in non-autono mous PDE- and PDAE-based systems remains a fundamental challenge, particularly in the presence of parameter uncertainty and measurement noise. In this study, we introduced a physics-based learning framework, BMINN, to systematically bridge this gap. By embedding physics-based formulations within Bayesian neural networks, BMINN learns unmodeled components together with their associated uncertainties, providing robust interpretability and predictive accuracy. Unlike purely data-driven approaches that map inputs to outputs, BMINN incorporates physically meaningful states and parameters by design, enabling the recovery of latent thermodynamics and dynamical rules.

Applied to lithium–graphite electrodes, BMINN reconstructs electrode-specific Gibbs free energies and chemical potentials directly from routine cycling data. The learned thermodynamics capture staging structures, transient liquid-like phases, and free-energy barriers, reproducing population dynamics and yielding *operando* XRD–comparable signatures of phase transitions. This capability provides a thermodynamically consistent description of metastable states and hysteresis, offering new insights into the microscopic origins of fast-charging limits and plating onset. Compared to OCP-fitted and PET-based models, the BMINN framework recovers a more accurate representation of internal states, with direct relevance to lifetime prognostics, aging-aware impedance modeling, and health-conscious control.

Beyond batteries, the framework exemplifies a general strategy for embedding physical models into Bayesian inference to recover hidden physics from input–output data. In this sense, BMINN establishes a pathway to uncover free-energy landscapes and governing functions in diverse systems where direct experimental access is limited, from catalytic surfaces and ferroic materials to other multiphase condensed-matter systems.

CRediT authorship contribution statement

Yicun Huang: Writing – review & editing, Writing – original draft, Visualization, Validation, Methodology, Investigation, Funding acquisition, Formal analysis, Conceptualization. **Qingbo Zhu:** Writing – review & editing, Visualization, Investigation, Formal analysis. **Torsten Wik:** Writing – review & editing, Writing – original draft, Supervision, Resources, Project administration, Methodology, Investigation, Formal analysis, Conceptualization. **Donal P. Finegan:** Writing – review & editing, Resources, Investigation, Data curation. **Yang Li:** Writing – review & editing, Investigation, Formal analysis, Conceptualization. **Changfu Zou:** Writing – review & editing, Writing – original draft, Visualization, Validation, Supervision, Resources, Project administration, Methodology, Investigation, Funding acquisition, Formal analysis, Data curation, Conceptualization.

Declaration of competing interest

The authors declare that they have no known competing financial interests or personal relationships that could have appeared to influence the work reported in this paper.

Appendix A. Supplementary data

Supplementary material related to this article can be found online at https://doi.org/10.1016/j.ensm.2026.104997.

Data availability

Data will be made available on request.

References

[1] D. Finegan, A. Quinn, D. Wragg, A. Colclasure, X. Lu, C. Tan, T. Heenan, R. Jervis, D. Brett, S. Das, T. Gao, D. Cogswell, M. Bazant, M. Michiel, S. Checcia, P. Shearing, K. Smith, Spatial dynamics of lithiation and lithium plating during high-rate operation of graphite electrodes revealed by operando optical microscopy, Energy Environ. Sci. 13 (8) (2020) 2570–2584, http://dx.doi.org/10.1039/d0ee01191f.

[2] C. Schmitt, A. Kube, N. Wagner, C. Friedrich, Understanding the influence of temperature on phase evolution in graphite during charge and discharge: An operando X-ray diffraction study, ChemElectroChem 9 (2) (2022) e202101342, http://dx.doi.org/10.1002/celc.202101342.

[3] J. Li, Q. Xu, Z. Luo, A. Cabot, Co–sn nanocrystalline solid solutions as anode materials in lithium-ion batteries with high pseudocapacitive contribution, ChemSusChem 12 (7) (2019) 1451–1458, http://dx.doi.org/10.1002/cssc.201802662.

[4] C.P. Grey, W.-S. Yoon, NMR studies of cathode materials for lithium-ion rechargeable batteries, Nat. Mater. 3 (3) (2004) 147–154, http://dx.doi.org/10.1038/nmat1078.

[5] W. Dreyer, J. Jamnik, C. Guhlke, R. Huth, J. Moškon, M.G. cek, The thermodynamic origin of hysteresis in insertion batteries., Nat. Mater. 95 (2010) 448–453.

[6] M.Z. Bazant, Theory of chemical kinetics and charge transfer based on nonequilibrium thermodynamics, Acc. Chem. Res. 46 (5) (2012) 1144–1160.

[7] W. Rüdorff, U. Hofmann, Über graphitsalze, Z. Anorg. Allg. Chem. 238 (1938) 1–50.

[8] N. Daumas, A. Herold, Relations between phase concept and reaction mechanics in graphite insertion compounds, Comptes Rendus Hebd. Des Seances L Acad. Des Sci. Ser. C 268 (5) (1969) 373.

[9] N.J.J. de Klerk, A. Vasileiadis, R.B. Smith, M.Z. Bazant, M. Wagemaker, Explaining key properties of lithiation in TiO_2-anatase li-ion battery electrodes using phase-field modeling, Phys. Rev. Mater. 1 (2017) 025404.

[10] R.B. Smith, E. Khoo, M.Z. Bazant, Intercalation kinetics in multiphase-layered materials, J. Phys. Chem. C 121 (2017) 12505–12523.

[11] M. Chandesris, D. Caliste, D. Jamet, P. Pochet, C. B'erthier, Thermodynamics and related kinetics of staging in intercalation compounds, J. Phys. Chem. C 123 (38) (2019) 23711–23720, http://dx.doi.org/10.1021/acs.jpcc.9b05298.

[12] M. Rykner, M. Chandesris, Free energy model for lithium intercalation in graphite: Focusing on the coupling with graphene stacking sequence, J. Phys. Chem. C 126 (12) (2022) 5457–5472.

[13] G. Ombrini, M. Wagemaker, M.Z. Bazant, W.C. Chueh, G. Singh, Thermodynamics of multi-sublattice battery materials revealed by an extended regular solution model, Npj Comput. Mater. 9 (1) (2023) 115, http://dx.doi.org/10.1038/s41524-023-01109-1.

[14] A. Pozzato, M. Ferrari, M.Z. Bazant, N. Marzari, S. Bo, Hybrid physics–machine learning framework for path-dependent two-phase battery electrode dynamics, Npj Comput. Mater. 10 (1) (2024) 197, http://dx.doi.org/10.1038/s41524-024-01197-7.

[15] J. Asenbauer, T. Eisenmann, M. Kuenzel, A. Kazzazi, Z. Chen, D. Bresser, The success story of graphite as a lithium-ion anode material – fundamentals, remaining challenges, and recent developments including silicon (oxide) composites, Sustain. Energy Fuels 4 (2020) 5387–5416.

[16] X. Lu, D.P. Finegan, J.L. Fife, H. Wang, S. Zhang, K. Dai, M. Di Michiel, S. Checcia, K. Smith, D.J.L. Brett, P.R. Shearing, M.Z. Bazant, Multiscale dynamics of charging and plating in graphite electrodes coupling operando microscopy and phase-field modelling, Nat. Commun. 14 (1) (2023) 5127, http://dx.doi.org/10.1038/s41467-023-40574-6.

[17] Y. Guo, R.B. Smith, Z. Yu, D.K. Efetov, J. Wang, P. Kim, M.Z. Bazant, L.E. Brus, Li intercalation into graphite: Direct optical imaging and Cahn-Hilliard reaction dynamics., J. Phys. Chem. Lett. 7 (11) (2016) 2151–2156.

[18] R.B. Smith, M.Z. Bazant, Multiphase porous electrode theory, J. Electrochem. Soc. 164 (11) (2017) E3291.

[19] Y. Li, F.E. Gabaly, T.R. Ferguson, R.B. Smith, N.C. Bartelt, J.D. Sugar, K.R. Fenton, D.A. Cogswell, A.L.D. Kilcoyne, T. Tyliszczak, M.Z. Bazant, W.C. Chueh, Current-induced transition from particle-by-particle to concurrent intercalation in phase-separating battery electrodes., Nat. Mater. 13 (12) (2014) 1149–1156.

[20] J. Park, H. Zhao, S.D. Kang, K. Lim, C.-C. Chen, Y.-S. Yu, R.D. Braatz, D.A. Shapiro, J. Hong, M.F. Toney, M.Z. Bazant, W.C. Chueh, Fictitious phase separation in li layered oxides driven by electro-autocatalysis, Nat. Mater. 20 (2021) 991–999.

[21] M.Z. Bazant, Thermodynamic stability of driven open systems and control of phase separation by electro-autocatalysis, Faraday Discuss. 199 (2017) 423–463.

[22] H. Zhao, M.Z. Bazant, Population dynamics of driven autocatalytic reactive mixtures, Phys. Rev. E 100 (2019) 012144.

[23] D. Fraggedakis, N. Nadkarni, T. Gao, T. Zhou, Y. Zhang, Y. Han, R.M. Stephens, Y. Shao-Horn, M.Z. Bazant, A scaling law to determine phase morphologies during ion intercalation, Energy Environ. Sci. 13 (7) (2020) 2142–2152, http://dx.doi.org/10.1039/D0EE00653J.

[24] W. Dreyer, C. Guhlke, R. Huth, The behavior of a many-particle electrode in a lithium-ion battery, Phys. D: Nonlinear Phenom. 240 (2011) 1008–1019.

[25] D.P. Finegan, J. Zhu, X. Feng, M. Keyser, M. Ulmefors, W. Li, M.Z. Bazant, S.J. Cooper, The application of data-driven methods and physics-based learning for improving battery safety, Joule 5 (2021) 316–329.

[26] Y. Huang, C. Zou, Y. Li, T. Wik, MINN: Learning the dynamics of differential-algebraic equations and application to battery modeling, IEEE Trans. Pattern Anal. Mach. Intell. 46 (12) (2024) 11331–11344.

[27] S.L. Brunton, J.L. Proctor, J.N. Kutz, Discovering governing equations from data by sparse identification of nonlinear dynamical systems, Proc. Natl. Acad. Sci. 113 (2015) 3932–3937.

[28] M. Raissi, P. Perdikaris, G.E. Karniadakis, Physics informed deep learning (Part II): Data-driven discovery of nonlinear partial differential equations, 2017, ArXiv.

[29] M. Heß, P. Novák, Shrinking annuli mechanism and stage-dependent rate capability of thin-layer graphite electrodes for lithium-ion batteries, Electrochim. Acta 106 (2013) 149–158.

[30] M.W. Verbrugge, B. Koch, Modeling lithium intercalation of single-fiber carbon microelectrodes, J. Electrochem. Soc. 143 (1996) 600–608.

[31] S. Hess, A. Latz, S. Thiele, J. Zausch, J. Eller, H. D"oring, F. Holzer, I. Manke, V. Schmidt, A. Weber, In situ observation and mathematical modeling of lithium distribution within graphite, J. Electrochem. Soc. 164 (11) (2017) E3063–E3072, http://dx.doi.org/10.1149/2.0061711jes.

[32] T. Gao, D.A. Cogswell, M.Z. Bazant, Interplay of lithium intercalation and plating on a single graphite particle, Joule 5 (2) (2021) 393–414, http://dx.doi.org/10.1016/j.joule.2020.12.020.

[33] S. Lian, Q. Xu, J. Li, Z. Deng, Y. Yu, K.-H. Chen, Modeling lithium plating onset on porous graphite electrodes, J. Electrochem. Soc. 171 (1) (2024) 010526, http://dx.doi.org/10.1149/1945-7111/ad1e3d.

[34] M. Doyle, T.F. Fuller, J. Newman, Modeling of galvanostatic charge and discharge of the lithium/polymer/insertion cell, J. Electrochem. Soc. 140 (6) (1993) 1526–1533.

[35] A. Van der Ven, S. Auerbach, K. Smith, Hysteresis in electrochemical systems, Batter. Energy 1 (2) (2022) e20210017, http://dx.doi.org/10.1002/bte2.20210017.

[36] X. Li, T. Wei, Y. Bai, A. Pei, W. An, P. Zhang, Q. Xu, K.-H. Chen, Y. Liu, J.-G. Zheng, J. Huang, In-situ structural characterizations of electrochemical intercalation of graphite compounds, Carbon Energy 1 (2) (2019) 200–218, http://dx.doi.org/10.1002/cey2.29.

[37] J.S. Edge, S.E.J. O'Kane, R. Prosser, N. Kirkaldy, A.N. Patel, A. Hales, A. Ghosh, W. Ai, J. Chen, J. Yang, S. Li, M.-C. Pang, L.B. Diaz, A. Tomaszewska, M.W. Marzook, K. Radhakrishnan, H. Wang, Y. Patel, B. Wu, G.J. Offer, Lithium ion battery degradation: what you need to know, Phys. Chem. Chem. Phys. : PCCP 23 (14) (2021) 8200–8221.

[38] K.-H. Chen, F. Planella, K. O'Regan, D. Gastol, W.D. Widanage, E. Kendrick, Development of experimental techniques for parameterization of multi-scale lithium-ion battery models, J. Electrochem. Soc. 167 (8) (2020) 080534, http://dx.doi.org/10.1149/1945-7111/ab9050.

[39] G. Galuppini, M. Berliner, R.D. Braatz, M.Z. Bazant, Nonlinear identifiability analysis for multiphase porous-electrode models of $lifePO_4$, J. Power Sources 573 (2023) 233009, http://dx.doi.org/10.1016/j.jpowsour.2023.233009.

[40] D. Monasterial, D. Tang, S. Gopalakrishnan, M. Landstorfer, U. Aydemir, W. Tremel, J. Martin, Dynamic in-plane heterogeneous and inverted response of lithium-ion battery anodes during electrochemical insertion, Small Sci. 3 (7) (2023) 2200067, http://dx.doi.org/10.1002/smsc.202200067.

[41] A. Senyshyn, O. Dolotko, M.J. Mühlbauer, K. Nikolowski, H. Fuess, H. Ehrenberg, Lithium intercalation into graphitic carbons revisited: Experimental evidence for twisted bilayer behavior, J. Electrochem. Soc. 160 (2013) 3198.

[42] M. Welling, Y.W. Teh, Bayesian learning via stochastic gradient langevin dynamics, in: International Conference on Machine Learning, 2011.

[43] A. Klein, M. Sadd, N. Mozhzhukhina, M. Olsson, L. Broche, S. Xiong, A. Matic, Identifying the role of electrolyte additives for lithium plating on graphite electrode by operando X-ray tomography, Batter. Supercaps 7 (7) (2024) e202400070.

[44] N. Guo, S. Chen, J. Tao, Y. Liu, J. Wan, X. Li, Semi-supervised learning for explainable few-shot battery lifetime prediction, Joule 8 (6) (2024) 1820–1836.

[45] S. Zhao, S. Chen, J. Zhou, C. Li, T. Tang, S.J. Harris, Y. Liu, J. Wan, X. Li, Potential to transform words to watts with large language models in battery research, Cell Rep. Phys. Sci. 5 (3) (2024) 101844.

[46] T. Lu, X. Zhai, S. Chen, Y. Liu, J. Wan, G. Liu, X. Li, Robust battery lifetime prediction with noisy measurements via total-least-squares regression, Integration 96 (2024) 102136.

[47] C.R. Birkl, M.R. Roberts, E. McTurk, P.G. Bruce, D.A. Howey, Degradation diagnostics for lithium ion cells, J. Power Sources 341 (2017) 373–386.

[48] Y. Zhang, T. Wik, J. Bergstr"om, C. Zou, Machine learning-based lifelong estimation of lithium plating potential: A path to health-aware fastest battery charging, Energy Storage Mater. 74 (2025) 103877, http://dx.doi.org/10.1016/j.ensm.2024.103877.

[49] C. Fang, B. Lu, G. Pawar, M. Zhang, D. Cheng, S. Chen, M. Ceja, J.-M. Doux, H. Musrock, M. Cai, B. Liaw, Y.S. Meng, Pressure-tailored lithium deposition and dissolution in lithium metal batteries, Nat. Energy 6 (10) (2021) 987–994.